Laser and Particle Beams (2015), *33*, 405–413.

doi:10.1017/S0263034615000439

Dispersion analysis of the solid helical pulse-forming line

LANGNING WANG AND JINLIANG LIU

College of Optoelectronic Science and Engineering, National University of Defense Technology, Changsha, People's Republic of China

(RECEIVED 29 January 2015; ACCEPTED 28 March 2015)

Abstract

In this paper, a solid helical pulse-forming line (HPFL) is described. The electromagnetic (EM) dispersion theory is used to calculate the important parameters of the HPFL based on tape helix model. Dispersion effects on the important EM parameters of HPFL, such as electric length and characteristic impedances, are analyzed. When Al_2O_3 ceramic is applied to be the dielectric in the HPFL, the pulse width of the HPFL is calculated nearly 50 ns only with the length of 305 mm. EM field simulation can draw the dispersion curve of the HPFL directly, which can describe the dispersion effect on the electric length of HPFL. Furthermore, the EM field simulation and experiments are carried out to verify the theoretical calculations of the pulse wide and characteristic impedances. Both simulation and experimental results can prove the EM analyses and calculations in this paper.

Keywords: Ceramic; Dispersion theory; Helical pulse-forming line; Tape helix

1. INTRODUCTION

Compact, portable pulsed power systems are required for modern applications (Joler *et al.*, 2002; Gundersen *et al.*, 2003; Jiang *et al.*, 2004; 2005). Pulse-forming line (PFL) is one of the basic elements of a pulsed power system. Conventionally, it is feasible to build high-voltage long-pulse pulsed power generators using liquid dielectric such as transformer oil or water in PFL (Korovin *et al.*, 2001; Yang *et al.*, 2009). Currently, solid ceramic dielectrics have been widely investigated as potential, attractive candidates in compact, portable pulsed power systems, as they can behave in a high dielectric constant and high breakdown strength at the same time (Sharma *et al.*, 2011; Su *et al.*, 2014). In particular, compared with transformer oil, ceramic dielectric material commonly has a larger dielectric constant about a few tens to a few thousands, of which the bulk breakdown strength is also high up to 100 kV/cm (Xia *et al.*, 2008; Zhang *et al.*, 2010). Besides, there is no other subsidiary equipment adopted for long time and large numbers repetitive running, which is important when water is used with characteristics of a strong polarity and low resistivity (Zhang *et al.*, 2013).

Although ceramic is an ideal dielectric for compact and portable PFLs, large ceramic bulks are difficult to manufacture (Xia *et al.*, 2008). Many researches are focused on the volume effect of solid material breakdown (Decup *et al.*, 2009; Neusel & Schneider 2014), which is a major difficulty in using ceramic lines at high-power level. Hence, the solid state PFLs are often built as small planar structure and stacked in the Blumlein or Marx form to generate a long-width, high-power pulse (Nunnally *et al.*, 2005; Wang *et al.*, 2013*a*). Unfortunately, the surface flashover often occurs at high voltage in planar lines, when bulk breakdown strength is not achieved (Wang *et al.*, 2013*b*). On the other hand, planar lines are an "open" structure, which the coupling between lines will decrease the efficiency of voltage multiplication (Korioth, 1998). It is possible to solve these problems by designing PFL of other structure. Unlike planar structure, the possibility of surface flashover in coaxial structure line is lower for the fewer flashover ways. Moreover, the helical structure can be employed to increase pulse width of PFL.

The tape helix is first used in the helical-type traveling wave tubes as an ideal slow-wave structure with good dispersion characteristics and broad transmission band (Kompfner 1947; Johnson *et al.*, 1956). Since 1980s, the tape helix has been introduced in the field of pulsed power technology to construct electron accelerator based on helical pulse-forming line (HPFL) (Teranishi *et al.*, 1991; Korovin *et al.*, 2001; Liu *et al.*, 2006), so that the pulse duration of the accelerator can be scaled up to several hundred numbers range, while the size of PFL decreased.

The "quasi-static" transmission circuit method is the common used method for characteristic parameters analysis

Address correspondence and reprint requests to: Langning Wang, College of Optoelectronic Science and Engineering, National University of Defense Technology, Changsha 410073, People's Republic of China. E-mail: wanglangning@126.com

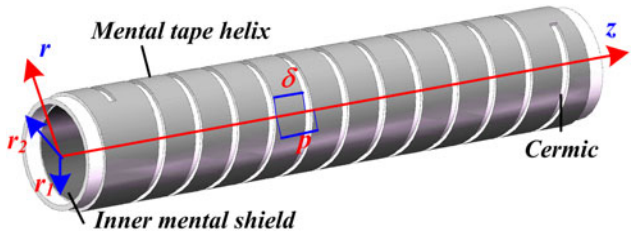

Fig. 1. The tape-helix structure of HPFL.

of the helical PFL (Johnson *et al.*, 1956; Liu *et al.*, 2007). But this method always employs parameters without dispersion to describe the HPFL which does have dispersion, so that the method has errors. Electromagnetic (EM) dispersion theory for the helical slow wave structure, including helical sheath method and tape helix model, can be used to analyze the HPFL (Stark 1954; Kino & Paik, 1962; Kartikeyan *et al.*, 1999). However, in the helical sheath method, the effects from tape width and other local geometric structures are still not clear, so that the spatial harmonic components in the EM field cannot be calculated. It is also difficult to calculate the characteristic impedances and pulse width, influenced by the spatial harmonics in the PFL. By contrast, the tape helix model is able to analyze the dispersion of HPFL and calculate the characteristic impedances, pulse width, and field proportions of spatial harmonics (D'Agostino *et al.*, 1998; Dialetis *et al.*, 2009). Recently, Zhang and Liu (2012); Zhang *et al.* (2011; 2012*a*; 2012*b*) have used the tape helix model to analyze the helical dispersion Blumlein transmission line successfully.

In this study, a solid HPFL has been constructed. At first, the characteristic impedances, pulse width, and dispersion curve of the HPFL are calculated by the EM dispersion theory based on the tape helix model. Then, the calculation is verified by CST microwave simulation. At last, some low-voltage test results on the HPFL are introduced.

2. HPFL STRUCTURE AND ITS DISPERSION MODEL

Cylindrical coordinates (r, θ, z) of the slow-wave structure are established along the axial direction (z) as shown in Figure 1. r and θ represent the radial and azimuthal directions. r_1 and r_2 represent the radii of the inner shield, outer tape helix, respectively. δ and p are the tape width and the pitch, respectively. ψ is the pitch angle and l is the length of the tape in the axial direction. Geometric parameters of the HPFL are shown in Table 1. If $l \gg r_2$, the slow-wave system can be viewed as infinite long. Considering the ideal boundary conditions of the metal shields, only two regions are divided to analyze the EM fields distribution, such as Region I ($r_1 < r < r_2$) and Region II ($r_2 < r$). The ceramic material fills in Region I, and the relative permittivity and permeability of the filling ceramic are ϵ_1 and μ_1, respectively. For the dielectric in outer space (Region II), the relative permittivity $\epsilon_2 = 1$ and permeability $\mu_2 = 1$. In our simulation and tests, the ceramics material is Al_2O_3, of which the relative permittivity $\epsilon_1 = 9.3$ and permeability $\mu_1 = 1$.

Table 1. *Geometric parameters of the helical PFL*

r_1 (mm)	r_2 (mm)	δ (mm)	p (mm)	l (mm)
26.5	33.5	20	25	305

In the PFL based on the tape helix, the pitch p and tape width δ are of a finite size, and the distance between the adjacent tape turns cannot be neglected (Zhang & Liu, 2012). Under these conditions, the helical sheath model which neglects the mini-structures (p and δ) brings in an error. Therefore, with the help of tape helix model, the EM field distribution and dispersion equation of the HPFL are calculated in the section of Appendix as Eqs. (A3) and (A4), and (A8), respectively.

3. ANALYSIS OF DISPERSION CURVE AND EM PARAMETERS

3.1. Dispersion Curve

For a square PFL with pulse duration as τ, the main part of the spectrum of the formed square pulse is in [0, 1/τ], according to Fourier transformation results. In other words, those EM components whose spectrums are outside [0, 1/τ] have negligible contributions to the formed square pulse. So, the approximate work band of the PFL is about [0, 1/τ]. Especially, the main frequency band can be estimated as [0, 20 MHz] for a 50 ns range PFL. From the calculation of Appendix as Eq. (A8), the dispersion Eq. (1) consists of infinite terms of Bessel functions (n_0 is infinite).

$$\omega = \frac{1}{\sin(\psi)}\left\{\frac{\sum_{n=-n_0}^{n_0}\left(\frac{[\cos(\psi)-\beta_n n\sin(\psi)/(\gamma_n^2 r_2)]^2\gamma_n}{\varepsilon_2\varepsilon\left[K'_{n2}/K_{n2}\right]-\varepsilon_1\varepsilon\left[(I'_{n2}K_{n1}-I_{n1}K'_{n2})/I_{n2}K_{n1}-I_{n1}K_{n2}\right]}\right)\left(\left[(\text{bessel}\,J_0(\beta_n\delta/2))/(\text{bessel}\,J_0(\beta_0\delta/2))\right]\right)^2}{\sum_{n=-n_0}^{n_0}\left(\left\{(\mu/\gamma_n)/(\left[K_{n2}/K'_{n2}\right]-\left[(I_{n2}K'_{n1}-I'_{n1}K_{n2})/I'_{n2}K'_{n1}-I'_{n1}K'_{n2}\right])\right\}\right)\left(\left[(\text{bessel}\,J_0(\beta_n\delta/2))/(\text{bessel}\,J_0(\beta_0\delta/2))\right]\right)^2}\right\}^{\frac{1}{2}} \quad (1)$$

https://doi.org/10.1017/S0263034615000439 Published online by Cambridge University Press

According to Eq. (A6), the coefficient A_{10} of the zeroth spatial harmonic ($n = 0$) is about several degrees larger than the coefficients A_{11} of high-order spatial harmonics ($n = 1$). Furthermore, A_{1n} becomes smaller when n becomes larger. So, we would guess that the EM field of high-order spatial harmonics occupies very small proportions in the total EM field in the HPFL, and the EM dispersion characteristics of the HPFL are almost determined by the zeroth harmonic. To prove our assumption, the dispersion curve with different number of the spatial harmonics according to Eq. (1) is plotted as shown in Figure 2. There are two major features in Figure 2. That is to say, the curve of $n_0 = 20$ coincides with the curve of $n_0 = 50$ and the three curves partly coincide under low frequency.

Under this low-frequency condition of the HPFL, the fundamental harmonic determines the dispersion characteristics of the HPFL as shown in Figure 2. In view of that, only the zeroth term in dispersion Eq. (1) can be considered, so the dispersion relation of the zeroth harmonic is obtained as Eq. (2), in which

$$\begin{cases} \omega = \pm\gamma_0 \cot\psi T_0(\gamma_0) \\ T_0(\gamma_0) = \left\{ \dfrac{(I_{02} - [I_{01}/K_{01}]K_{02})[(-[I_{11}/K_{11}][I_{12}/K_{12}])K_{02} - (I_{02} + [I_{11}/K_{11}]K_{02})]}{\mu(I_{12} - [I_{11}/K_{11}]K_{12})[\varepsilon_2\varepsilon K_{12}([I_{01}/K_{01}] - [I_{02}/K_{02}]) - \varepsilon_1\varepsilon(I_{12} + [I_{01}/K_{01}]K_{12})]} \right\}^{\frac{1}{2}} \end{cases} \tag{2}$$

Actually, dispersion relation (2) shows the dispersion characteristics of the HPFL in the first "Brillouin zone" ($-\pi < \beta_0$, $p < \pi$). According to Eq. (A1), the periodical helical slow-wave system has periodical dispersion relation. Using Eqs. (A1) and (2), the periodical dispersion relation of the HPFL is given as

$$\omega(\beta p) = \omega(\beta_0 p + 2\pi n), \quad n = 0, \pm1, \pm2, \pm3, \ldots \tag{3}$$

Using the data in Table 1 and the dispersion relation in Eq. (3), the dispersion curve of all the spatial harmonics in the HPFL is plotted as shown in Figure 3.

Generally speaking, the field is almost only determined by the fundamental harmonic, and the higher-order spatial harmonics can be ignored. So, the important parameter like the characteristic impedances of the HPFL can be analyzed just by considering the dispersion curve in the first Brillouin zone.

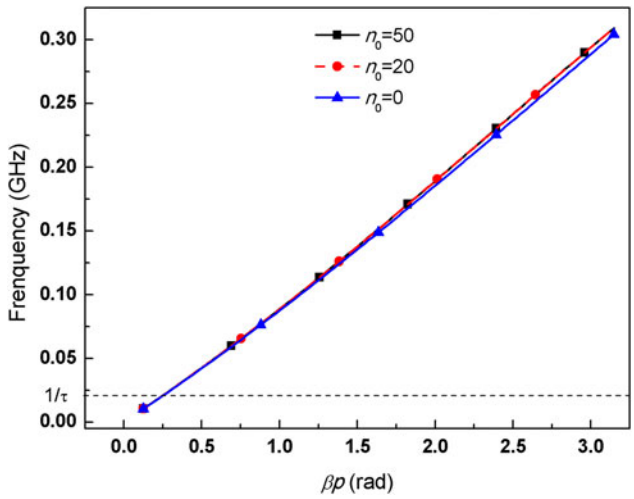

Fig. 2. Dispersion curves with different number of n_0.

3.2. EM Parameters of HPFL

As the dispersion characteristics of the designed HPFL are almost determined by the fundamental harmonic in the first Brillouin zone, the analyses of the HPFL can be simplified by a large extent. In this section, the characteristic impedances (Z) and electric length (τ_0) are calculated in the section of Appendix as Eqs. (A9)–(A11). According to Eq. (4) and data in Table 1, the important EM parameters of the HPFL are presented in Figure 4. As we know, the pulse width (τ) is twice as the electric length (τ_0).

$$\begin{cases} \tau_0 = l/v_{\text{ph}} = l\beta/\omega, \ \ \tau = 2\tau_0 \\ Z = \dfrac{\beta_0(I_{01}K_{02} - I_{02}K_{01})}{\gamma_0^2 K_{01} M_{10\text{in}}} \end{cases} \tag{4}$$

In Figure 4a, the electric length of the HPFL is presented. The electric length of the HPFL almost keeps constant when frequency (f) increases, which shows that the dispersion has

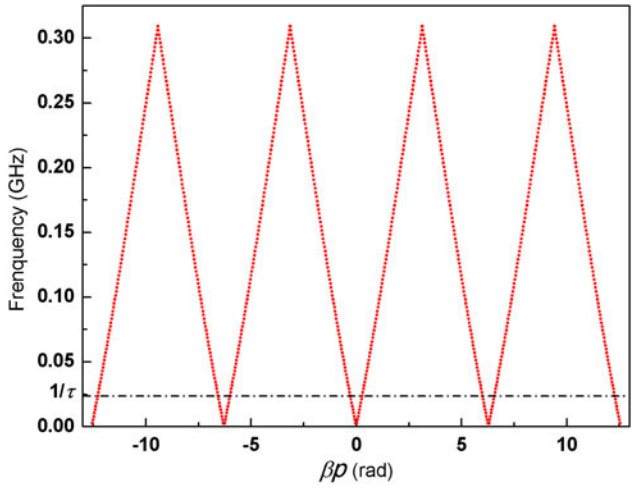

Fig. 3. Dispersion curve of the spatial harmonics of the HPFL.

https://doi.org/10.1017/S0263034615000439 Published online by Cambridge University Press

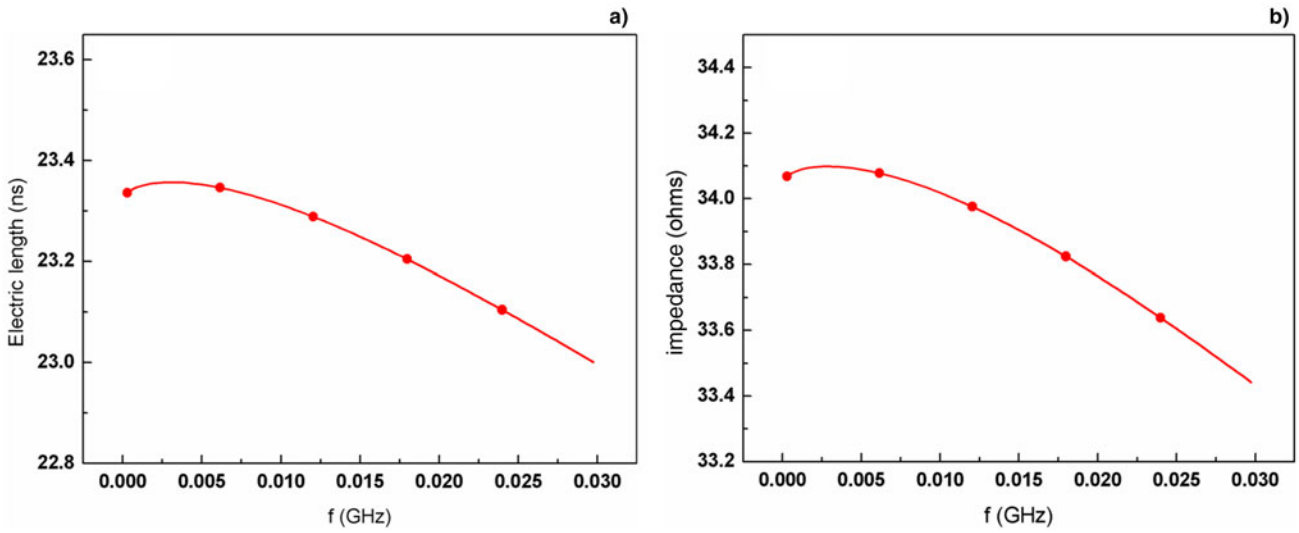

Fig. 4. Important characteristic parameters of the HPFL. (a) Electric length of the PFL (τ_0) versus frequency (f); (b) characteristic impedance (Z) versus frequency (f).

very few effects on the pulse width. Figure 4a also shows that the main frequency band can be estimated as [0, 20 MHz]. In Figure 4b, the characteristics impedances of the zeroth spatial harmonic of the HPFL decrease little when frequency (f) increases under the main frequency band.

4. EM SIMULATION BY CST SOFT

4.1. Dispersion Curve

Codes of CST MICROWAVE STUDIO suite can be employed to simulate the dispersion curve of the periodical slow-wave structure. The dispersion curves calculated by CST show a good agreement with theory calculations as shown in Figure 5.

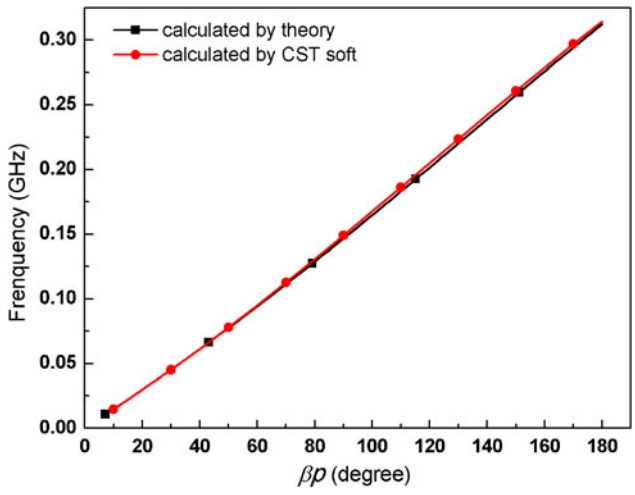

Fig. 5. Comparison between the dispersion curves calculated by CST and by theory for the HPFL when $0 < \beta_0 p < \pi$.

4.2. Pulse-forming simulation

In order to obtain the pulse-forming characteristic of the HPFL, we have built a transient model of pulse-forming system using the CST MWS co-simulation tool (Wang *et al.*, 2015). The geometric model, circuit schematic, and the waveform of current through 33 Ω load are shown in Figure 6. Before the time of 890 ns, the HPFL is charged through the DC voltage source 1 and the voltage-control switch is open. Pulse voltage source 2 is set to control the switch closing in the time of 890 ns, so the HPFL begins to be discharged in the matched resistance at the rest of time as shown in Figure 6c.

In Figure 6c, the waveform of voltage on HPFL is reduced to half, which shows that the matching resistance of HPFL is nearly 33 Ω. Additionally, the current pulse is of 50 ns pulse width. These results show a good agreement between the simulation and theory calculations as shown in Figure 4.

5. EXPERIMENTAL RESULTS

5.1. Delay Time Measurement

In order to testify the theoretical calculation and simulation results of the electric length which describe the phase velocity and dispersion characteristics of the HPFL, the principle of the delay time measurement is as follows.

The signal source is employed to generate the pulse with 50 ns pulse width. Then, the signal is divided to two channel (CH1 and CH2), one of which is connected to the oscilloscope directly and the other of which is connected to the oscilloscope through the HPFL. By measuring the time gap between the two channels in the oscilloscope, we can get the delay time. However, that delay time is not equal to the

https://doi.org/10.1017/S0263034615000439 Published online by Cambridge University Press

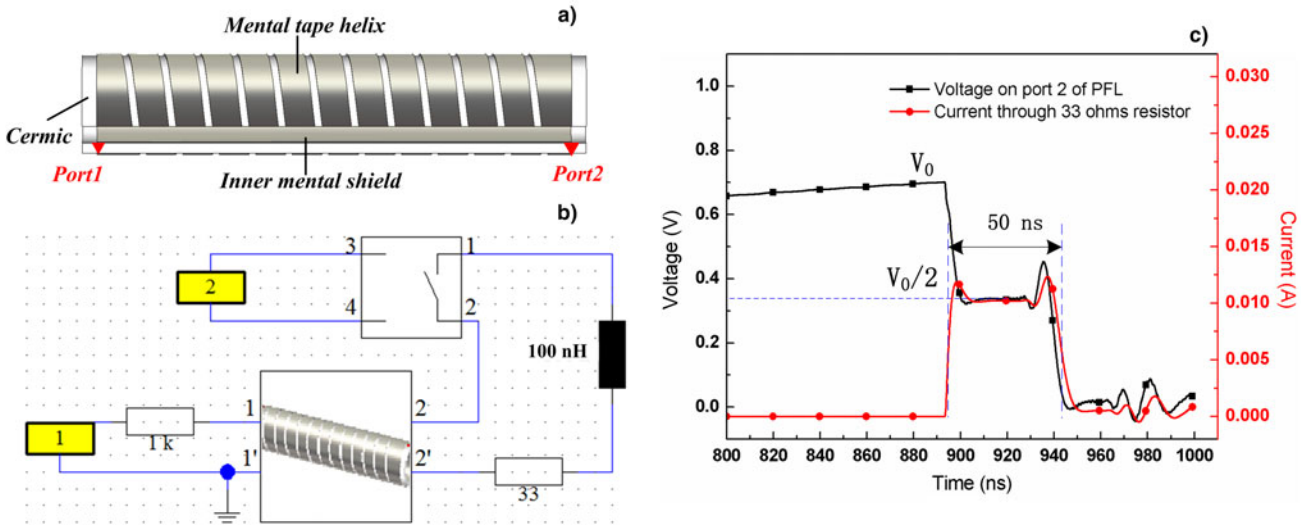

Fig. 6. CST simulation model of pulse-forming system and the formed voltage pulse by HPFL. (a) Geometric model of HPFL in co-simulation; (b) CST co-simulation model of the pulse-forming circuit; (c) the waveforms of voltage on port2 of HPFL and the load current pulse.

electric length of the HPFL, since the delay time is equal to the sum of the electric length and the origin time gap of two channels. Therefore, two time gaps need to be carried out for measuring the delay time of the HPFL, including the time gap with HPFL and the time gap without HPFL. In Figure 7b, we put the waveforms of two tests together in one figure and make the two CH2 waveform lines overlap. At this time, the delay time is the time gap between two CH1 waveforms, which is 24 ns as shown in Figure 7b, which means that the theoretical calculation of electric length of the HPFL is correctly shown in Figure 4b.

In Figure 7b, we could find that the CH1 and CH2 waveforms are different in one test, no matter whether the HPFL is added in the measurement circuit, while the two CH1 and CH2 without the HPFL waveforms are similar to the CH1 and CH2 with the HPFL, respectively. It is because that the CH2 channels consist of two 50 Ω coaxial line each with two clamps to connect the HPFL as shown in Figure 7a. When the HPFL is not added in the measurement circuit, the two coaxial lines are clamped together by the two clamps. The clamps bring mismatching to the 50 Ω coaxial line, which can generate a reflect pulse into CH1 channel. That is why the CH1 and CH2 waveforms are different in one test.

5.2. Pulse-forming Test under Low Voltage

For the purpose of testifying the theoretical calculations of the characteristic impedances and pulse width of the HPFL, experimental system of a pulse-forming platform was built

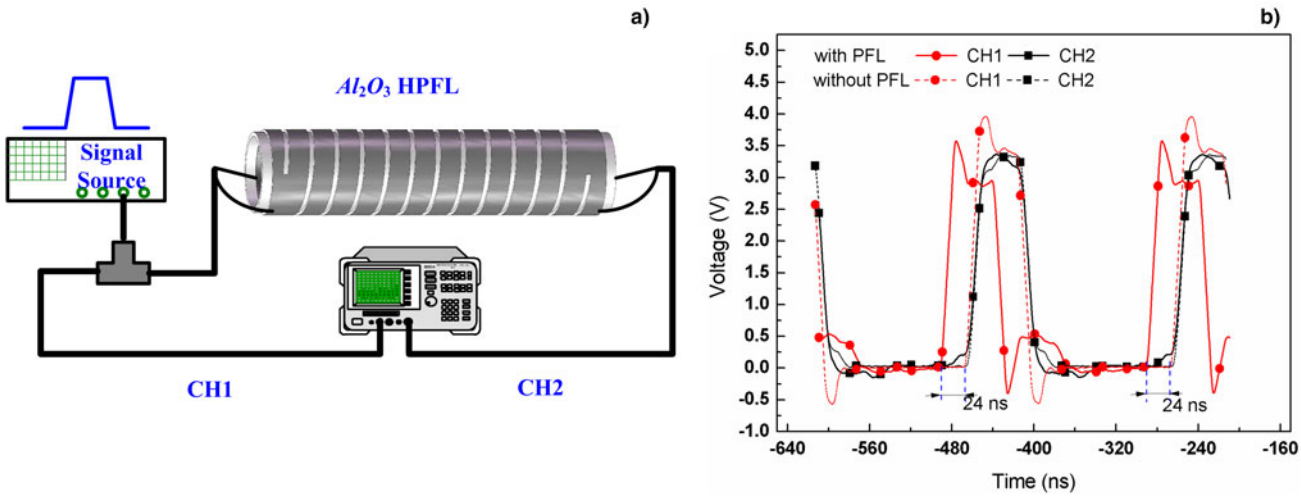

Fig. 7. Test platform for delay-time measurements (a) and the waveforms of signals (b).

https://doi.org/10.1017/S0263034615000439 Published online by Cambridge University Press

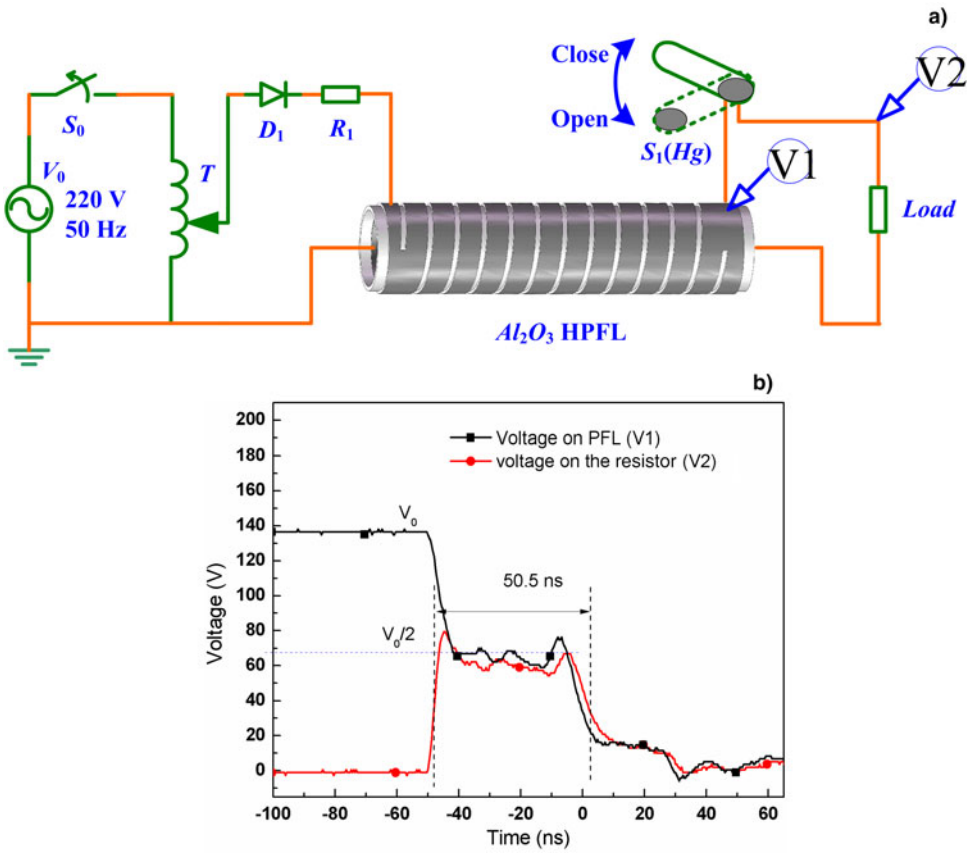

Fig. 8. Test platform of the pulse-forming system (a) and the waveforms of voltage on HPFL and the load (b).

up as shown in Figure 8a. The system consisted of a voltage regulator (T), a silicon diodes, a 10 kΩ current-limiting water resistance (R_1), HPFL, a mercury switch (S_1), a matched load (33 Ω). The working process is as follows. Firstly, the HPFL is charged up to 100 V. Then, the HPFL is discharged to the 33 Ω load through the switch and a pulse is obtained on the load.

In Figure 8b, the waveform of voltage on PFL is reduced to half, which suggests that the matching resistance of the HPFL is nearly 33 Ω. Additionally, the pulse obtained on the resistor is of 50 ns pulse width. These experimental results show a good agreement with the simulation results as shown in Figure 6.

6. CONCLUSIONS

Recent technological advances have directed further research toward reduction in dimensions of pulse power system to a portable scale. In our study, a compact, portable ceramic helical PFL is designed and analyzed by the dispersion theory. The tape-helix model is introduced to analyze the effects of dispersion on the important EM parameters of HPFL. Dispersion effects on the important EM parameters of PFL, such as electric length and characteristic impedances, are also analyzed in detail. EM field simulation and experiments are carried out to testify the theoretical calculations well. At present, the Al_2O_3 HPFL can deliver a pulse with 50 ns width. In fact, if the other high breakdown strength solid dielectrics (Jue *et al.*, 2007; Chung *et al.*, 2008; Chen *et al.*, 2011) with a greater relative permittivity were chosen, the pulse width would be greater. As a unit of multi-PFL, we can stack it as the Marx form to increase the output power. These works mentioned above will be done in the future.

ACKNOWLEDGMENT

We gratefully acknowledge the support from Shananxi Baoguang Ceramic Science & Technology Co., Ltd in the manufacturing of this Al_2O_3 HPFL.

REFERENCES

Chen, G.H., Zhang, W.J., Liu, X.Y. & Zhou, C.R. (2011). Preparation and properties of strontium barium niobate based glass-ceramics for energy storage capacitors. *J. Electroceram.* **27**, 78–82.

Chung, U., Elissalde, C., Maglione, M., Estournès, C., Pate, M. & Ganne, J.P. (2008). Low-losses, highly tunable Ba 0.6 Sr 0.4 TiO_3/MgO composite. *Appl. Phys. Lett.* **92**, 042902–042902.

D'Agostino, S., Emma, F. & Paoloni, C. (1998). Accurate analysis of helix slow-wave structures. *IEEE Trans. Electron Devices* **45**, 1605–1613.

https://doi.org/10.1017/S0263034615000439 Published online by Cambridge University Press

Decup, M., Malec, D. & Bley, V. (2009). Impact of a surface laser treatment on the dielectric strength of α-alumina. *J. Appl. Phys.* **106**, 094103–094104.

Dialetis, D., Chernin, D., Antonsen, T.M. & Levush, B. (2009). Accurate representation of attenuation in helix TWT simulation codes. *IEEE Trans. Electron Devices* **56**, 935–944.

Gundersen, M., Dickens, J. & Nunnally, W. (2003). Compact, portable pulsed power: physics and applications. *14th IEEE Int. Pulsed Power Conf.* **1**, 9–12.

Jiang, W., Oshima, N., Yokoo, T., Yatsui, K., Takayama, K., Wake, M., Shimizu, N. & Tokuchi, A. (2005). Development of repetitive pulsed power generators using power semiconductor devices. *IEEE Pulsed Power Conf.*, pp. 1167–1172.

Jiang, W., Yatsui, K., Takayama, K., Akemoto, M., Nakamura, E., Shimizu, N., Tokuchi, A., Rukin, S., Tarasenko, V. & Panchenko, A. (2004). Compact solid-state switched pulsed power and its applications. *Proc. IEEE* **92**, 1180–1196.

Johnson, H.R., Everhart, T.E. & Siegman, A.E. (1956). Wave propagation on multifilar helices. *IEEE Trans. Dielectr. Electr.* **2**, 18–24.

Joler, M., Christodoulou, C., Gaudet, J., Schamiloglu, E., Schoenbach, K., Joshi, R. & Laroussi, M. (2002). Study of high energy storage Blumlein transmission lines as high power microwave drivers (No. 2002-01-3179). SAE Technical Paper.

Jue, W., Ping, Y. & Bin, L. (2007). High energy density dielectrics for Transmission Line. *34th IEEE Int. Conf. on Plasma Science*, pp. 388–388..

Kartikeyan, M.V., Sinha, A.K., Bandopadhyay, H.N. & Venkateswarlu, D.S. (1999). Effective simulation of the radial thickness of helix for broad band, practical TWT's. *IEEE Trans. Plasma Sci.* **27**, 1115–1123.

Kino, G.S. & Paik, S.F. (1962). Circuit theory of coupled transmission systems. *J. Appl. Phys.* **33**, 3002–3008.

Kompfner, R. (1947). Traveling wave tube as amplifier at microwaves. *Proc. IRE* **35**, 124–127.

Korioth, J.L. (1998). *A computational analysis of stacked Blumlein pulse generators*. Ph.D. Thesis, University of Texas.

Korovin, S.D., Gubanov, V.P., Gunin, A.V., Pegel, I.V. & Stepchenko, A.S. (2001). Repetitive nanosecond high-voltage generator based on spiral forming line. *IEEE Int. Pulsed Power Conf.*, Vol. **2**, pp. 1249–1251.

Liu, J., Li, C., Zhang, J., Li, S. & Wang, X. (2006). A spiral strip transformer type electron-beam accelerator. *Laser Part. Beams* **24**, 355–358.

Liu, J., Yin, Y., Ge, B., Cheng, X., Feng, J., Zhang, J. & Wang, X. (2007). A compact high power pulsed modulator based on spiral Blumlein line. *Rev. Sci. Instrum.* **78**, 103302.

Neusel, C. & Schneider, G.A. (2014). Size-dependence of the dielectric breakdown strength from nano-to millimeter scale. *J. Mech. Phys. Solids* **63**, 201–213.

Nunnally, W.C., Lewis, R., Allen, F., Hawkins, S., Holmes, C., Sampayan, S. & Caporaso, G. (2005). Experiments with UV laser triggered spark gaps in a stacked Blumlein system. *15th IEEE Int. Pulsed Power Conf.*, pp. 1376–1381.

Scotto, M.J. & Parzen, P. (1956). The electronic theory of tape-helix traveling-wave structures. *IRE Trans. Electron Devices* **3**, 160–160.

Sharma, S.K., Deb, P., Shukla, R., Prabaharan, T. & Shyam, A. (2011). Compact pulse forming line using barium titanate ceramic material. *Rev. Sci. Instrum.* **82**, 115102.

Stark, L. (1954). Lower modes of a concentric line having a helical inner conductor. *J. Appl. Phys.* **25**, 1155–1162.

Su, J., Zhang, X., Li, R., Zhao, L., Sun, X., Wang, L., Zeng, B., Cheng, J., Wang, Y., PENG, J., & Song, X. (2014). An 8-GW long-pulse generator based on Tesla transformer and pulse forming network. *Rev. Sci. Instrum.* **85**, 063303.

Teranishi, T., Nojima, K., Motegi, S., Murase, H.H., Ohshima, I., Shidara, T., Akernoto, M., Takeda, S. & Takata, K. (1991). A 600 kV Blumlein modulator for an X-band klystron. *8th IEEE Int. Pulsed Power Conf.*, pp. 315–318.

Tien, P.K. (1953). Traveling-wave tube helix impedance. *Proc. IRE* **41**, 1617–1623.

Wang, L., Liu, J. & Feng, J. (2015). A compact 100 kV high voltage glycol capacitor. *Rev. Sci. Instrum.* **86**, 014701.

Wang, S., Shu, T. & Yang, H. (2013*a*). Note: A 3-stage stacked Blumlein using ceramic for energy storage. *Rev. Sci. Instrum.* **84**, 026104.

Wang, S., Shu, T., Zhang, J., Zhang, Z. & Yang, H. (2013b). Breakdown characteristics of Niobate glass-ceramic under pulsed condition. *IEEE Trans. Dielectr. Electr. Insul.* **20**, 275–280.

Xia, L., Zhang, H., Shi, J., Zhang, H., Deng, J., Liu, H. & Cao, M. (2008). A compact, portable pulse forming line. *Rev. Sci. Instrum.* **79**, 086113.

Yang, H., Xu, J., Zhang, J., Zhong, H., Wang, Y., Fan, Y., Zhang, Z., Yang, J., Luo, L. & Zhao, Y. (2009). Experiments of a 30 GW, 100 ns Compact E-beam accelerator. *2009 IET European Pulsed Power Conf.*, pp. 1–4.

Zhang, H.B., Yang, J.H., Gao, F. & Lin, J.J. (2013). Experimental study of the breakdown characteristic of glycerol as energy storage medium in pulse forming line. *2013 IEEE Conf. on Electrical Insulation and Dielectric Phenomena (CEIDP)*, pp. 850–853.

Zhang, Q., Wang, L., Luo, J., Tang, Q. & Du, J. (2010). Ba0. 4Sr0. $6TiO_3$/MgO composites with enhanced energy storage density and low dielectric loss for solid-state pulse-forming line. *Int. J. Appl. Ceram. Technol.* **7**(s1), E124–E128.

Zhang, Y. & Liu, J.L. (2012). Impedance matching condition analysis of the multi-filar tape-helix Blumlein PFL with discontinuous dielectrics. *Laser Part. Beams* **30**, 639–650.

Zhang, Y., Liu, J., Fan, X., Zhang, H., Wang, S. & Feng, J. (2011). Characteristic impedance and capacitance analysis of Blumlein type pulse forming line of accelerator based on tape helix. *Rev. Sci. Instrum.* **82**, 104701.

Zhang, Y., Liu, J., Wang, S., Fan, X., Zhang, H. & Feng, J. (2012a). Effects of dielectric discontinuity on the dispersion characteristics of the tape helix slow-wave structure with two metal shields. *Laser Part. Beams* **30**, 329–339.

Zhang, Y., Liu, J.L. & Feng, J.H. (2012b). Effects of dispersion on electromagnetic parameters of tape-helix Blumlein pulse forming line of accelerator. *The Eur. Phys. J. Appl. Phys.* **57**, 30904.

APPENDIX

CALCULATIONS OF DISPERSION EQUATIONS

The EM field and its excitation surface current density J are both in periodical distribution, due to the helical symmetry of the tape helix. If $l \gg r_2$, the EM field and J both consist of their own spatial harmonic components according to the

https://doi.org/10.1017/S0263034615000439 Published online by Cambridge University Press

Floquet theorem (Scotto & Parzen, 1956). In these spatial harmonics, the axial phase constant β_n of the nth harmonic is related to β_0 (phase constant of the fundamental harmonic) as Eq. (A1)

$$\beta_n = \beta_0 + 2\pi n/p \tag{A1}$$

As the source of the EM field, the excitation surface current on the tape helix has many distribution models. In this paper, the current model in (Scotto & Parzen, 1956; Tien, 1953) is adopted. That is to say, (1) the magnitude of the current density is taken as becoming infinitely large in an inverse square root manner as the tape edges are approached and is zero in the gap between helical conductors; and (2) the phase constant phase contour of the current is normal to the edge of the helical tape. The surface current density consists of two of which one is in parallel with the helical direction ($J_{//}$) and the other is normal to the helical direction ($J_{\perp} = 0$). Then, $J_{//}$ can also be calculated by the Floquet theorem as

$$\begin{cases} J_{//} = \mathrm{e}^{-j(\beta_0 z-\omega t)} \sum\limits_{n=-\infty}^{+\infty} \left(J_{//n} \mathrm{e}^{-jn\left(\frac{2\pi}{p} z-\theta\right)} \right) \\ \qquad = \mathrm{e}^{j\omega t} \sum\limits_{n=-\infty}^{+\infty} (J_{//n} \mathrm{e}^{-jn(\beta_n z-\theta)}) \\ |J_{//n}| = \left| \dfrac{\text{bessel}\, J_0(\beta_n \delta/2)}{\text{bessel}\, J_0(\beta_n \delta/2)} J_{//0} \right| \end{cases} \tag{A2}$$

In Eq. (A2), besslJ_0 represents the 0-order solution of Bessel J function. "j" is unit of imaginary number, n is the order number of the spatial harmonic, ω is the angular frequency of the nth harmonic. By solving the Maxwell equations, the analytical solutions of EM field in Regions I and II are as follows.

EM field in Region I ($r_1 < r < r_2$) as

$$\begin{cases} E_{1z} = \mathrm{e}^{-j(\beta_0 z-\omega t)} \sum\limits_{n=-\infty}^{+\infty} (A_{1n} I_{nr} + A_{2n} K_{nr}) \mathrm{e}^{-jn(2\pi z/p-\theta)} \\ H_{1z} = \mathrm{e}^{-j(\beta_0 z-\omega t)} \sum\limits_{n=-\infty}^{+\infty} (A_{3n} I_{nr} + A_{4n} K_{nr}) \mathrm{e}^{-jn(2\pi z/p-\theta)} \\ E_{1r} = \mathrm{e}^{-j(\beta_0 z-\omega t)} \sum\limits_{n=-\infty}^{+\infty} \left[\dfrac{j\beta_n}{\gamma_n} (A_{1n} I'_{nr} + A_{2n} K'_{nr}) - \dfrac{\omega\mu n}{\gamma_n^2 r} (A_{3n} I_{nr} + A_{4n} K_{nr}) \right] \mathrm{e}^{-jn(2\pi z/p-\theta)} \\ E_{1\theta} = \mathrm{e}^{-j(\beta_0 z-\omega t)} \sum\limits_{n=-\infty}^{+\infty} \left[\dfrac{-n\beta_n}{\gamma_n^2 r} (A_{1n} I_{nr} + A_{2n} K_{nr}) - \dfrac{j\omega\mu}{\gamma_n} (A_{3n} I'_{nr} + A_{4n} K'_{nr}) \right] \mathrm{e}^{-jn(2\pi z/p-\theta)} \\ H_{1r} = \mathrm{e}^{-j(\beta_0 z-\omega t)} \sum\limits_{n=-\infty}^{+\infty} \left[\dfrac{\omega\varepsilon_1 \varepsilon n}{\gamma_n^2 r} (A_{1n} I_{nr} + A_{2n} K_{nr}) + \dfrac{j\beta_n}{\gamma_n} (A_{3n} I'_{nr} + A_{4n} K'_{nr}) \right] \mathrm{e}^{-jn(2\pi z/p-\theta)} \\ H_{1\theta} = \mathrm{e}^{-j(\beta_0 z-\omega t)} \sum\limits_{n=-\infty}^{+\infty} \left[\dfrac{j\omega\varepsilon_1 \varepsilon}{\gamma_n} (A_{1n} I'_{nr} + A_{2n} K'_{nr}) - \dfrac{\beta_n n}{\gamma_n^2 r} (A_{3n} I_{nr} + A_{4n} K_{nr}) \right] \mathrm{e}^{-jn(2\pi z/p-\theta)} \end{cases} \tag{A3}$$

The EM field in Region II ($r > r_2$) as

$$\begin{cases} E_{2z} = \mathrm{e}^{-j(\beta_0 z-\omega t)} \sum\limits_{n=-\infty}^{+\infty} (B_{1n} I_{nr} + B_{2n} K_{nr}) \mathrm{e}^{-jn(2\pi z/p-\theta)} \\ H_{2z} = \mathrm{e}^{-j(\beta_0 z-\omega t)} \sum\limits_{n=-\infty}^{+\infty} (B_{3n} I_{nr} + B_{4n} K_{nr}) \mathrm{e}^{-jn(2\pi z/p-\theta)} \\ E_{2r} = \mathrm{e}^{-j(\beta_0 z-\omega t)} \sum\limits_{n=-\infty}^{+\infty} \left[\dfrac{j\beta_n}{\gamma_n} (B_{1n} I'_{nr} + B_{2n} K'_{nr}) - \dfrac{\omega\mu n}{\gamma_n^2 r} (B_{3n} I_{nr} + B_{4n} K_{nr}) \right] \mathrm{e}^{-jn(2\pi z/p-\theta)} \\ E_{2\theta} = \mathrm{e}^{-j(\beta_0 z-\omega t)} \sum\limits_{n=-\infty}^{+\infty} \left[\dfrac{-n\beta_n}{\gamma_n^2 r} (B_{1n} I_{nr} + B_{2n} K_{nr}) - \dfrac{j\omega\mu}{\gamma_n} (B_{3n} I'_{nr} + B_{4n} K'_{nr}) \right] \mathrm{e}^{-jn(2\pi z/p-\theta)} \\ H_{2r} = \mathrm{e}^{-j(\beta_0 z-\omega t)} \sum\limits_{n=-\infty}^{+\infty} \left[\dfrac{\omega\varepsilon_2 \varepsilon n}{\gamma_n^2 r} (B_{1n} I_{nr} + B_{2n} K_{nr}) + \dfrac{j\beta_n}{\gamma_n} (B_{3n} I'_{nr} + B_{4n} K'_{nr}) \right] \mathrm{e}^{-jn(2\pi z/p-\theta)} \\ H_{2\theta} = \mathrm{e}^{-j(\beta_0 z-\omega t)} \sum\limits_{n=-\infty}^{+\infty} \left[\dfrac{j\omega\varepsilon_2 \varepsilon}{\gamma_n} (B_{1n} I'_{nr} + B_{2n} K'_{nr}) - \dfrac{\beta_n n}{\gamma_n^2 r} (B_{3n} I_{nr} + B_{4n} K_{nr}) \right] \mathrm{e}^{-jn(2\pi z/p-\theta)} \end{cases} \tag{A4}$$

https://doi.org/10.1017/S0263034615000439 Published online by Cambridge University Press

In Eqs. (A3) and (A4), and ϵ and μ are the permittivity and permeability, respectively. A_{1n}~A_{4n} and B_{1n}~B_{4n} are field coefficients which need to be calculated. I_n and K_n are the modified Bessel functions of the first and second kinds, respectively. k and γ_n are the angular wave number and the phase constant in the transverse direction, and $\gamma_n^2 = \beta_n^2 - k^2$.

If the inner are ideal conductors and outer space is infinite, their boundary conditions are given as

$$\begin{cases} E_{1z} = 0, E_{1\theta} = 0 (r = r_1) \\ E_{2z} = 0, E_{2\theta} = 0 (r = \infty) \end{cases} \tag{A5}$$

The boundary conditions of tape helix are shown as

$$\begin{cases} E_{1z} = E_{2z}, E_{1\theta} = E_{2\theta} \\ H_{2z} - H_{1z} = -J_{//} \sin\psi, H_{2\theta} - H_{1\theta} = J_{//} \cos\psi (r = r_2) \\ \int_{S2} (\overline{E}_{//} \cdot \overline{J}^*_{//}) \, \mathrm{d}S_2 = 0 \end{cases} \tag{A6}$$

Using field Eqs. (A3), (A4) and boundary conditions of (A5) and (A6), the field coefficients can be calculated as (A7)

$$\begin{cases} A_{1n} = \dfrac{\gamma_n J_{//n}}{j\omega} \dfrac{[\cos(\psi) - \beta_n n \sin(\psi)/(\gamma_n^2 r_2)] K_{n1} K_{n2}}{\varepsilon_2 \varepsilon K'_{n2}(I_{n2}K_{n1} - I_{n1}K_{n2}) - \varepsilon_1 \varepsilon K_{n2}(I'_{n2}K_{n1} - I_{n1}K'_{n2})} \\ A_{3n} = \dfrac{-J_{//n} \sin(\psi) K'_{n1} K'_{n2}}{K_{n2}(I'_{n2}K'_{n1} - I'_{n1}K'_{n2}) - K'_{n2}(I_{n2}K'_{n1} - I_{n1}K'_{n2})} \\ A_{2n} = -A_{1n} I_{n1}/K_{n1}, A_{4n} = -A_{3n} I'_{n1}/K'_{n1} \\ B_{1n} = 0, B_{2n} = \dfrac{I_{n2}K_{n1} - I_{n1}K_{n2}}{K_{n1}K_{n2}} A_{1n} \\ B_{3n} = 0, B_4 = \dfrac{(I'_{n2}K'_{n1} - I'_{n1}K'_{n2})}{K'_{n1}K'_{n2}} A_{3n} \end{cases} \tag{A7}$$

In Eq. (A7), I_{n1} and I_{n2} are the simplified forms of $In(\gamma_n r_1)$ and $In(\gamma_n r_2)$, respectively, so do K_{n1} and K_{n2}. I'_{n2} represents the derivative of $In(\gamma_n r)$ to $\gamma_n r$ when $r = r_2$, so does K'_{n2}.

The transmitted waves determined by the EM fields are shown as Eqs. (A3) and (A4). According to Eqs. (A3), (A4) and the last equation in Eq. (A6), the dispersion equation of the helical PFL based on tape helix can be obtained as

$$\sum_{n=-\infty}^{+\infty} \left\{ \left\{ \begin{array}{c} \dfrac{\gamma_n [\cos(\psi) - \beta_n n \sin(\psi)/(\gamma_n^2 r_2)]^2 K_{n2}(I_{n2}K_{n1} - I_{n1}K_{n2})}{\omega[\varepsilon_2 \varepsilon K'_{n2}(I_{n2}K_{n1} - I_{n1}K_{n2}) - \varepsilon_1 \varepsilon K_{n2}(I'_{n2}K_{n1} - I_{n1}K'_{n2})]} \\ + \dfrac{\omega\mu \sin^2(\psi) K'_{n2}(I'_{n2}K'_{n1} - I'_{n1}K'_{n2})}{\gamma_n [K_{n2}(I'_{n2}K'_{n1} - I'_{n1}K'_{n2}) - K'_{n2}(I_{n2}K'_{n1} - I'_{n1}K_{n2})]} \end{array} \right\} (J_{//n} J^*_{//n}) \right\} = 0 \tag{A8}$$

In Eq. (A8), $J_{//n} J^*_{//n}$ can be substituted as the last equation in Eq. (A2). The dispersion equation consists of infinite terms of Bessel functions.

If we integrate $H_{1\theta}$ [in Eq. (A3)] along a closed circle which just encloses the tape helix in the azimuthal direction, current I_{zin} can be calculated as

$$\begin{cases} -I_{zin} = j \sum\limits_{n=-\infty}^{+\infty} A_{1n} M_{1n} \\ M_{10} = \dfrac{2\pi r_2 \omega \varepsilon_1 \varepsilon}{\gamma_0} \left(I'_{02} - \dfrac{I_{01}}{K_{01}} K'_{02} \right) \end{cases} \tag{A9}$$

Large quantities of terms of Bessel functions are included in Eq. (A9), so that it is difficult to solve this complicated equation. However, as we analyzed before, the EM dispersion characteristics of the HPFL are almost determined by the zeroth harmonic at low-frequency band. In addition, M_{10} can be obtained by setting $n = 0$ as Eq. (A9).

Then, we calculate the potential by integrating the zeroth harmonic E_{1r} from r_1 to r_2 as

$$\varphi = -\int_{r_1}^{r_2} E_{1r}(r)|_{n=0} \mathrm{d}r = -\frac{j\beta_0 A_{10}(I_{02}K_{01} - I_{01}K_{02})}{\gamma_0^2 K_{01}} \tag{A10}$$

At last, the characteristic impedances of the HPFL can be calculated as

$$Z = \frac{\varphi}{-I_{zin}} = \frac{\beta_0 (I_{01}K_{02} - I_{02}K_{01})}{-\gamma_0^2 K_{01} M_{10}} \tag{A11}$$

https://doi.org/10.1017/S0263034615000439 Published online by Cambridge University Press